Bioorganic Chemistry 103 (2020) 104188

Contents lists available at ScienceDirect

Bioorganic Chemistry

journal homepage: www.elsevier.com/locate/bioorg

Molecular modelling guided design, synthesis and QSAR analysis of new small molecule non-lipid autotaxin inhibitors

Souvik Banerjee[a,b,c,*], Derek D. Norman[b], Shanshan Deng[c], Sayo O. Fakayode[a], Sue Chin Lee[b], Abby L. Parrill[d], Wei Li[c], Duane D. Miller[c,*], Gabor J. Tigyi[b,*]

[a] Department of Physical Sciences, University of Arkansas Fort Smith, Fort Smith, AR 72913, USA
[b] Department of Physiology, College of Medicine, University of Tennessee Health Science Center, Memphis, TN 38163, USA
[c] Department of Pharmaceutical Sciences, College of Pharmacy, University of Tennessee Health Science Center, Memphis, TN 38163, USA
[d] Department of Chemistry, Computational Research on Material Institute, The University of Memphis, Memphis, TN 38152, USA

ARTICLE INFO

Keywords:
ATX
LPAR1 inhibitor
Sulfonamide
Tetrahydropyran
Morpholine
QSAR
PCA
Molecular docking

ABSTRACT

The lysophospholipase D autotaxin (ATX) generates lysophosphatidic acid (LPA) that activates six cognate G-protein coupled receptors (GPCR) in cancerous cells, promoting their motility and invasion. Four novel compounds were generated aided by molecular docking guided design and synthesis techniques to obtain new dual inhibitors of ATX and the lysophosphatidic acid receptor subtype 1 (LPAR1). Biological evaluation of these compounds revealed two compounds, **10** and **11**, as new ATX enzyme inhibitors with potencies in the range of 218–220 nM and water solubility (> 100 μg/mL), but with no LPAR1 inhibitory activity. A QSAR model was generated that included four newly designed compounds and twenty-one additional compounds that we have reported previously. The QSAR model provided excellent predictability of the pharmacological activity and potency among structurally related drug candidates. This model will be highly useful in guiding the synthesis of new ATX inhibitors in the future.

1. Introduction

In recent years there has been extensive research on autotaxin (ATX), a member of the ectonucleotide pyrophosphatase phosphodiesterase (ENPP) enzyme family (a.k.a. ENPP2), which is responsible for catalyzing the hydrolysis of lysophosphatidyl choline (LPC) and similar lysophospholipids to a growth-factor like bioactive phospholipid, lysophosphatidic acid (LPA) [1–13]. On the cell surface, LPA acts via six transmembrane G-protein coupled receptors, $LPAR_{1\text{-}6}$ (LPAR), to promote a variety of physiological responses, including cell proliferation, migration, motility, survival, and platelet aggregation [6,7,13–15]. Thus, the ATX-LPA signaling pathway has been considered to be at the core of a number of diseases, including fibrotic diseases, cardiovascular diseases, inflammation, and central pain [6,7,10,13,16,17]. In cancer cell biology, the ATX-LPA axis has been found to regulate malignant transformation, invasion, metastasis, and therapeutic resistance [1,4,6,10,13,18–21]. Additionally, ATX has been observed to play a critical role in proliferation and survival of ovarian as well as breast cancer stem cells [13,22–24].

The obvious involvement of LPA in the pathobiology of cancer has led to intensive research to develop drug-like ATX inhibitors. Various synthetic efforts have provided access to primarily two different kinds of ATX inhibitors: Lipidlike ATX inhibitors, mimicking LPC or LPA, and non-lipid ATX inhibitors [6,13,25]. Lipid-like ATX inhibitors have limited success in preclinical development mainly due to their high partition coefficient (logP > 5) [6]. Resolution of ATX co-crystal structure provided insight into the active surface of the enzyme [1,3]. A number of research groups, including ours, have carried out molecular modelling-guided rational drug discovery resulting in several new generations of small molecule non-lipid autotaxin inhibitors with pharmacological characteristics obeying Lipinski's rule of five. Most of the small molecule ATX inhibitors possess an acid or acid-like moiety that interact with the Zn^{2+} ions at the active site, a core spacer, and a hydrophobic tail [6,13,25]. However, to the best of our knowledge, none of these active site inhibitors have advanced to clinical development. Thus, recently there have been efforts to develop small molecule ATX inhibitors without an acid-like moiety that behave as allosteric modulators of the enzyme [6,13].

Galapagos has generated a small molecule non-lipid ATX inhibitor, GLPG1690 (Fig. 1), without a carboxylic acid functionality targeting the hydrophobic pocket of the enzyme [6,13,26,27]. The Galapagos compound has ATX inhibitory IC_{50} values in the range of 100 nM to

* Corresponding authors at: Department of Physical Sciences, University of Arkansas Fort Smith, Fort Smith, AR 72913, USA (S. Banerjee).
E-mail addresses: souvik.banerjee@uafs.edu (S. Banerjee), dmiller@uthsc.edu (D.D. Miller), gtigyi@uthsc.edu (G.J. Tigyi).

https://doi.org/10.1016/j.bioorg.2020.104188
Received 15 May 2020; Received in revised form 18 July 2020; Accepted 4 August 2020
Available online 26 August 2020

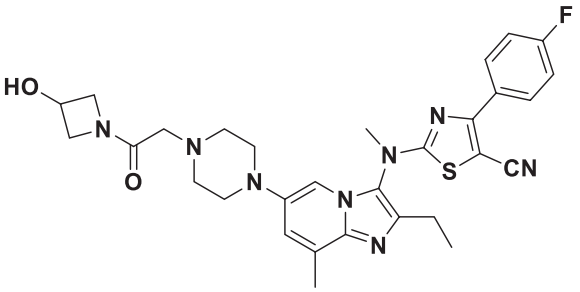

Galapagos 1690
ATX IC_{50}: 130-500 nM
Galapagos Inc.
Molecular Weight: 588.69
logP = 4.87

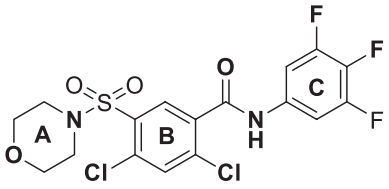

1, ATX Inhibitor, ATX IC_{50}: 9 nM,
LPAR1 IC_{50}: 14 μM
Molecular Weight: 469.26
logP = 3.23
J. Med. Chem. **2017**, *60*, 1309-1324

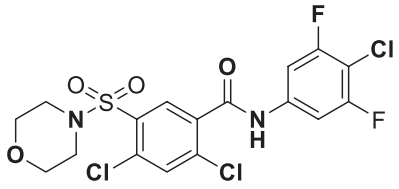

2, ATX Inhibitor, ATX IC_{50}: 84 nM,
LPAR1 IC_{50}: 6 μM
Molecular Weight: 485.71
logP = 3.23
J. Med. Chem. **2017**, *60*, 1309-1324

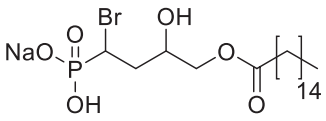

BrP-LPA, ATX/LPA1 Dual Inhibitor, ATX IC_{50}: 800 nM,
LPAR1 IC_{50}: 273 nM
Cancer Res. **2009**, *69*, 5441-5449

Fig. 1. Recently developed non-lipid small molecule ATX inhibitors and a lipid dual inhibitor of the ATX/LPAR1 axis.

500 nM [6,13]. GLPG1690 is currently under phase III clinical trial for the treatment of idiopathic pulmonary fibrosis, but due to its side effects on the female reproductive system, trials must exclude women of reproductive age [27]. Recently, we have reported highly potent small molecule non-lipid ATX inhibitors, **1** (ATX IC_{50}: 9 nM, Fig. 1) and **2,** (ATX IC_{50}: 84 nM, Fig. 1) targeting the hydrophobic pocket of the enzyme [13]. The inhibitor compound **1** is highly efficient in overcoming chemotherapeutic resistance of breast cancer stem-like cells and significantly inhibits B16F10 melanoma metastasis *in vivo* [13]. Additionally, both **1** and **2** behave as weak yet specific antagonists of LPAR1 G-protein coupled receptor (**1**: LPAR1 IC_{50} 14 μM; **2**: LPAR1 IC_{50}: 6 μM) making them dual inhibitors of ATX and LPAR1. As the product of ATX is LPA, which activates six LPA GPCR, there is widespread interest in finding non-lipid small molecule antagonists of both ATX and LPAR [7,19].

One might expect that dual inhibitors of ATX and LPARs would be more effective in overcoming LPA mediated resistance to chemotherapy and radiation therapy. Previously, we have reported a lipid-like pan LPAR antagonist (BrP-LPA, Fig. 1), which is a nanomolar inhibitor of ATX as well [19]. Since compound **2** has moderate inhibition and **1** has weak inhibitory activity of LPAR1, we attempted to modify these two agents to develop a dual inhibitor of ATX/LPAR1 with useful inhibitory property for the ATX (IC_{50} < 250 nM) and improved efficacy for LPAR1 inhibition (IC_{50} < 800 nM) while simultaneously meeting Lipinski's rule of five. We have made use of recently solved ATX [1,3] as well as LPAR1 [28] (**PDB ID: 4Z35**) co-crystal structures to perform computational calculations in guiding the design of potential dual inhibitors of ATX and LPAR1 based on the **1** and **2** scaffolds. We have also prepared a quantitative structure–activity relationship (QSAR) based on our recently reported non-lipid small molecule ATX inhibitors [13] to be able to predict the biological activity of the newly designed and computationally validated compounds against ATX.

One of the challenges of small organic drug molecule synthesis in the rational design and discovery of new agents is the capability to prescreen and predict the potency and/or pharmacological activity of structurally related drug candidates. Synthesis of all possible combinations of structurally related drug candidates is challenging, time consuming, and labor intensive. QSAR analysis has been strategically utilized in rational drug design to address these challenges. QSAR analysis is particularly relevant for rapid screening of potential drug candidates in order to prepare lead compounds in rational drug design [29–37]. QSAR analysis also affords prediction of enzymatic activity and pharmacological activity of structurally related compounds prior to actual laboratory syntheses with high accuracy, reducing the cost and time of organic drug design and synthesis [38–40]. Moreover, the practical applications of a combined use of QSAR analysis, principal component analysis (PCA), regression analysis, and computational modelling in rational drug design has been extensively demonstrated [41–48]. We, therefore explored the possible combined use of QSAR, PCA, regression analysis and computational modelling for rational design of ATX inhibitors with potential LPAR1 inhibitory activity in this study.

2. Results and discussion

2.1. Docking of compound 1 in LPAR1 and ATX crystal structures to rationally design new analogues

We prepared the co-crystallized LPAR1 structure (PDB ID: 4Z35) using Schrödinger Molecule Modeling software. The LPAR1 ligand binding site has a top polar region consisting of Tyr34 and Lys39 (Fig. 2**A**). Tyr34 formed a hydrogen bond with the LPAR1 antagonist **ONO-9910539**, and Lys39 formed a hydrogen bond, as well as a salt bridge with **ONO-9910539**. The middle portion of the binding site has

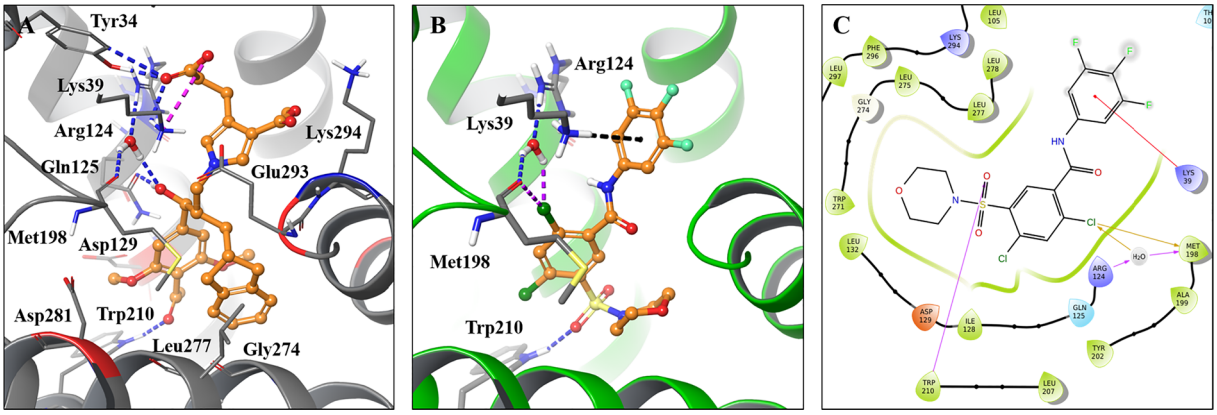

Fig. 2. Molecular modeling studies of compound **1** against the LPAR1 ligand binding site (**PDB ID: 4Z35**). (A) Detailed 3D structure of LPAR1 antagonist **ONO-9910539** (gold ball-and-stick model) and the LPAR1 receptor. The ribbon color represents the residue charge. Red ribbon indicates hydrogen acceptor region and blue ribbon represents hydrogen donor region. Hydrogen bond interaction is shown in blue dash line. Salt bridge is shown in pink dash line. (B) Ribbon representation of the docking pose of compound **1** (gold ball-and-stick model) with the LPAR1 binding site (green ribbon) (glide docking score of −6.25). Pi-cation interaction is shown in black dash line. Hydrogen bond is shown in blue dash line. Halogen bond is shown in purple dash line. (C) Two dimensional interaction panel of main residues involved in the molecular docking of compound **1** against LPAR1 receptor. (For interpretation of the references to color in this figure legend, the reader is referred to the web version of this article.)

a polar binding region on one surface, Arg124 and Gln125, with the other surface being a polar binding region with Glu293 and Lys294. Arg124 interacted with **ONO-9910539** through a water-mediated hydrogen bond, and Gln125 formed a hydrogen bond directly with the hydroxy functional group of **ONO-9910539**. The bottom of the ligand binding site has a polar surface with Asp129 and a further extended polar surface consisting of Asp281 and Trp210. Trp210 could form a hydrogen bond with the carbonyl group of the phenyl ring in **ONO-9910539**. Further, there was a hydrophobic surface on the other side of the bottom ligand binding site containing Gly274, Leu275 and Leu277. In general, the LPAR1 ligand binding surface is spherical with potential polar interactions at the top and middle, but the bottom region tends towards hydrophobic interactions. We designated three rings in compound **1** as rings A, B, and C (Fig. 1). To get an insight into the binding mode of compound **1** with the LPAR1 protein, we docked the it into the LPAR1 binding site (**PDB ID: 4Z35**) (Fig. 2**B and 2C**) and found that the dichloro-phenyl ring, ring B, was binding to the middle polar region of the LPAR1 binding site resulting in hydrophilic interactions with the Arg124 and Met198 via halogen bonds. The trifluoro-phenyl ring, ring C, was binding to the top polar region of the LPAR1 binding site through π-cation interaction with Lys39. The sulfonyl group of the sulfonamide linker and the morpholine, ring A, were close to the bottom polar region with Trp210 and bottom hydrophobic region with Gly274, respectively. Trp210 was predicted to form a hydrogen bond with the oxygen of the sulfonyl group. It is conceivable from Fig. 1**A** that there is more space to occupy and improve interactions near the top polar surface as well as the middle polar surface perpendicular to the middle phenyl ring, ring B. However, extension past the end of the aliphatic ring, ring A, may place the polar carboxy group in between polar and nonpolar receptor surfaces with significant solvent exposure. Thus, we decided to increase LPAR1 potency by replacing the sulfonamide with a larger polar functional group to better reach the bottom polar receptor surface, consisting of Trp210 and Asp281, while leaving the aliphatic ring, ring A, intact. Molecular docking of compound **1** against the ATX crystal structure (**PDB ID: 3NKM, Figure SI-1**) revealed that the substitution of the sulfonamide is limited in size, as ATX has less empty space around it than LPAR1 has (Fig. S1). In our previous study [13], we have designed compound **4a** (Fig. 3) with 5-morpholinoamino-sufonamide attaching to the middle dichloro-phenyl ring, ring B, to better reach out to the top polar surface. However, we have not had success in obtaining the desired compound **4a** from the intermediate **3**, as every attempt to prepare the methane-sulfonamide moiety has yielded compound **4b**. We have reported that neither intermediate **3** nor **4b** has ATX inhibitory activity. Our previous findings have demonstrated that the sulfonamide moiety is very important for interaction with the ATX binding pocket. Hence, we have now designed two new 4-aminotetrahydropyrano-sulfonamide analogues, compound **10** and compound **11** (Fig. 3). We have also designed a 4-cyanomethyl-morpholino analogue, compound **14**, as well as a 4-acetoxy-morpholino analogue, compound **15**.

2.2. Chemical synthesis, biological evaluation and molecular docking analysis of designed compounds

Compounds **10** and **11** were synthesized following the strategy described in Scheme 1 with 72% and 76% yields, respectively. We started with commercially available 5-Bromo-2,4-dicholoro-benzoic acid (**5**) which had been converted into the methyl ester (**6**). The 4-amino-tetrahydropyrano group was then installed using Buchwald coupling to obtain compound **7**. The methyl-sulfonyl moiety was then added to the amine group using LDA as a base to obtain compound **8**. The ester group of compound **8** was hydrolyzed to obtain benzoic acid **9**, a common intermediate of compounds **10** and **11**. The compounds **10** and **11** were then synthesized from **9** following standard peptide coupling procedures. The compounds **10** and **11** were tested for ATX inhibitory activity (Table 1). Replacement of the 4-amino-morpholino group in compound **3** (IC_{50} > 1000 nM) with 4-amino-tetrahydropyrano-sulfonamide resulted in significant improvement in ATX inhibitory activity in compound **10** (IC_{50} = 219 nM) and compound **11** (IC_{50} = 218 nM). However, neither compound **10** nor compound **11** showed any LPAR1 inhibitory activity. Compounds **10** and **11** were docked into both ATX (3NKM) as well as LPAR1 (4Z35) crystal structures for potential interactions and activity validations. Consistently, molecular docking studies have suggested that the oxygen of aliphatic ring A of compound **10** forms a weak aromatic hydrogen bond with Trp254, and that trifluoro-phenyl ring C has a π-π stacking interaction with the residue His251 (Fig. 4**A**). The glide docking score of compound **10** was −7.38, which was similar to that of compound **1**, at −7.34. Similarly, compound **11** formed a halogen bond with residue Gly256 mediated by a water molecule, as well as a π-π stacking interaction with the residue Trp260 with a glide docking score of −6.94 (Fig. 4**B**). The sulfonamide group is very important in positioning the location of aliphatic ring A into the hydrophobic pocket of the ATX binding site. However, by replacing the sulfonyl group with a sulfonamide group, compound **10** lost the hydrogen bond interacting with Trp210 and halogen bond interactions between dichloro-phenyl ring B and nearby

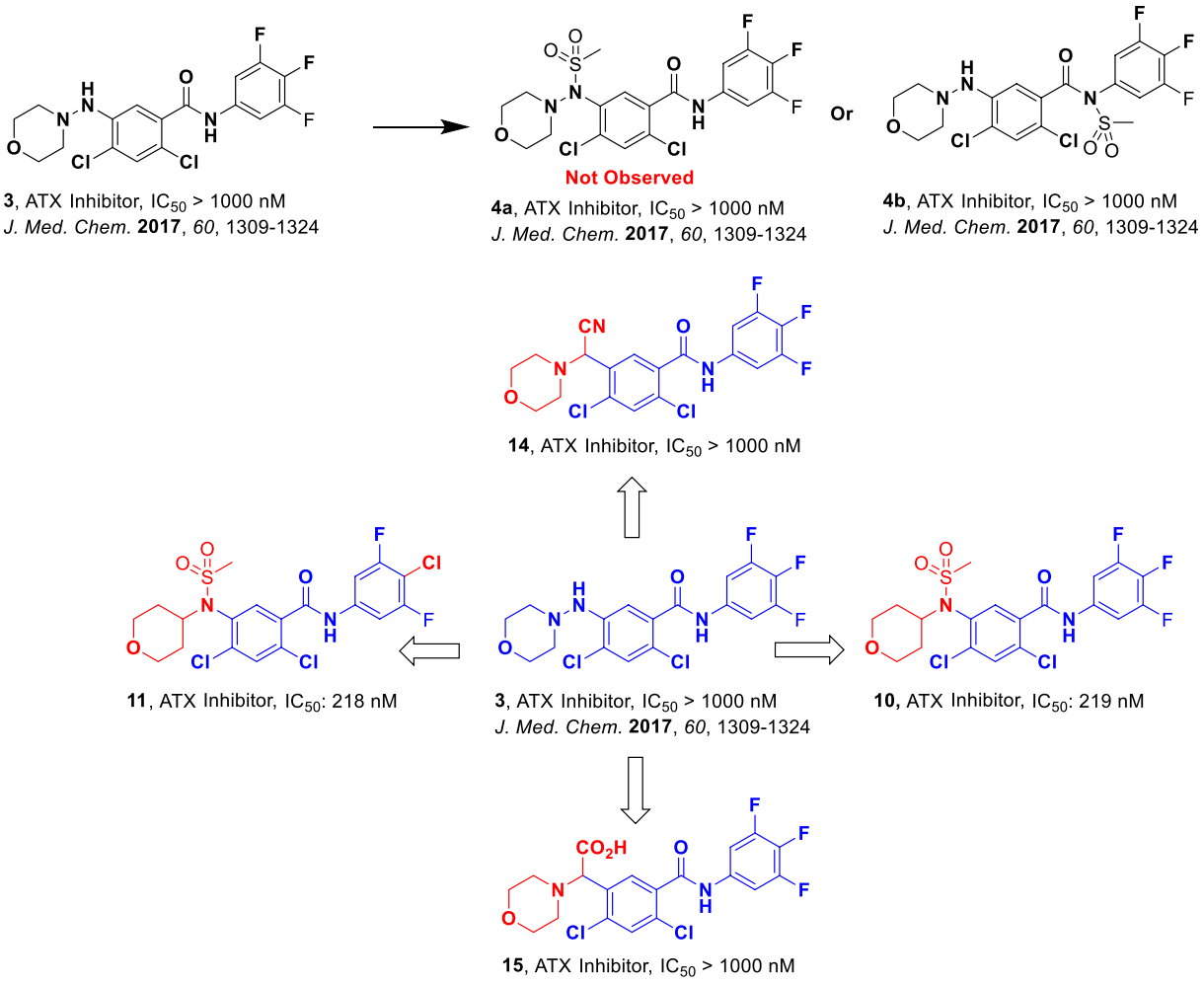

Fig. 3. Designed potential ATX/LPAR1 inhibitors for synthesis.

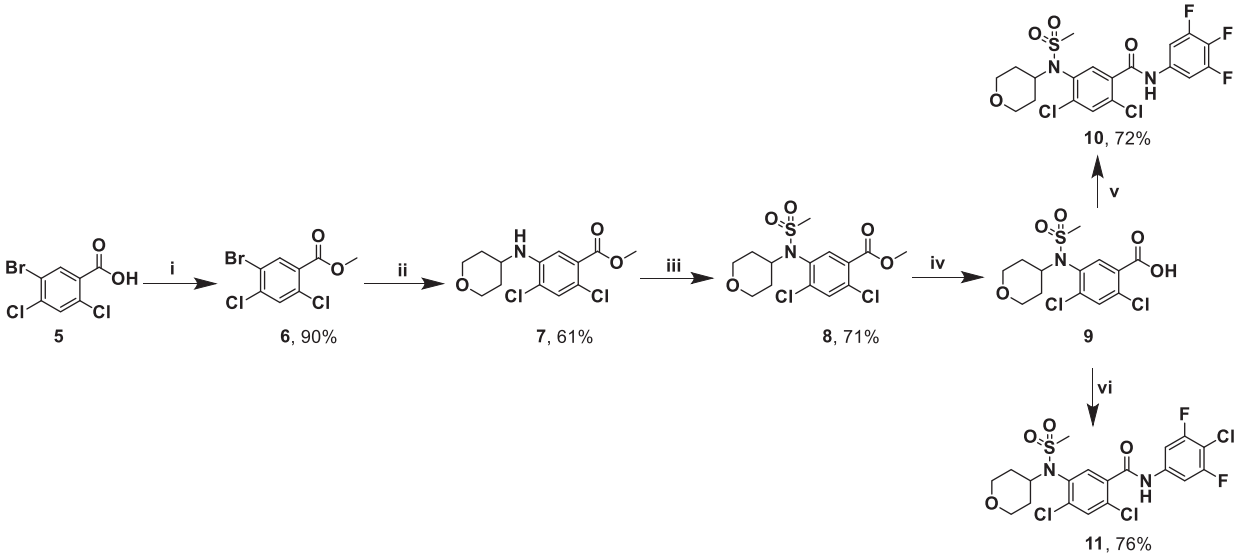

i. pTSA, CH_3OH, reflux; ii. 4-aminomorpholine, $Pd_2(dba)_3$, Xantphos, toluene, reflux; iii. CH_3SO_2Cl, LDA, THF, 0 ^{O}C; iv. LiOH, MeOH/H_2O (1:1), 12 hrs; v.a) $SOCl_2$, DMF (cat), CH_2Cl_2 (sol), 1 hr R.T. b) 3,4,5-Trifluoro-aniline, R.T. 12 hrs; vi. a) $SOCl_2$, DMF (cat), CH_2Cl_2 (sol), 1 hr R.T. b) 4-chloro-3,5-difluoro-aniline, R.T. 12 hrs

Scheme 1. Design and synthesis of 5-tetrahydropyrano-5-methanesulfonamido-aniline analogue.

Table 1
Enzyme inhibition data for the newly identified ATX inhibitors.

Compound	IC_{50} (nM ± SD) vs FS-3	pNP-TMP inhibition	Mechanism	log P	MW	Solubility (μg/mL)
10	219.6 ± 14.7	none	Competitive	3.2	497.31	> 100
11	218.9 ± 25.2	none	Competitive	3.68	513.76	> 100
14	> 1000	none	ND	2.91	393.34	50
15	> 1000	none	ND	2.44	412.34	> 100

ND = not determined.

residues in LPAR1 (Fig. 4**C**) causing the reduction of its docking score to −5.98. Although the docking score of compound **11** (−6.23) was equivalent to that of compound **1**, alteration of the sulfonamide group and a chlorine group in the trifluoro-phenyl ring C forced the horizontal flip of the aliphatic ring A, which might be the reason that compound **11** lost its inhibitory activity of LPAR1 (Fig. 4**D**).

To further improve polar-polar interactions with both ATX and LPAR1 polar surfaces, we synthesized compound **14** and the corresponding carboxylic acid compound **15** following the strategy as described in Scheme 2, with 78% and 65% yields respectively. We started with commercially available 2-fluoro-5-formyl benzoic acid to perform a Strecker synthesis using morpholine as the secondary amine and TMSCN as the source of nitrile to obtain the α-amino-nitrile **13**. The carboxylic acid moiety of compound **13** was then coupled with the 3,4,5-trifluoro-nitrile to obtain compound **14** in good yield. Eventually, compound **14** was hydrolyzed to yield the desired 2-(4-fluoro-3-((3,4,5-trifluorophenyl)carbamoyl)phenyl)-2-morpholinoacetic acid, **15**. Compounds **14** and **15** showed no detectable biological activity against ATX or LPAR1 (IC_{50}s > 1000 nM, Table 1). To provide further insight into our findings, compounds **14** and **15** were docked in the ATX (3NKM) as well as LPAR1 (4Z35) crystal structures. Compared to the reference compound **1**, the docking studies of compounds **14** against the ATX protein demonstrated that the hydrogen bond interaction disappeared when the sulfonyl group was replaced by a cyanomethyl group (Fig. 5**A**). In comparison to compound **1** docked in ATX crystal structure (Fig. SI-1), the alteration pushed topside of the structure of compound **14**, rotating it approximately 30° clockwise and bending the aliphatic ring A to the right, and pushing ring A away from the hydrophobic binding region comprised of Leu213 and Phe210. The rotation resulted in change of the amide carbonyl group from facing inside to facing outside, pushing it away from Trp260. All these effects contributed to a decreased glide docking score of −6.61 and reduced ATX inhibitory activity. Similarly, replacement of the sulfonyl group with the carboxylic acid group caused the structure of compound **15** to slightly rotate clockwise, and forced the amide carbonyl group away from Trp260, weakening the hydrogen bond between these moieties (Fig. 5**B**). In addition, rotation of the structure also pushed ring A to the right, leading to loss of the interactions with the hydrophobic residues of the pocket. The glide docking score of compound **15** was only −5.78, providing further evidence for the weak activity of compound **15** against ATX. In the co-crystallized LPAR1 protein, the substitution of the cyanomethyl group of compound **14** disrupted the dichloro-phenyl ring B from the top polar region consisting of Tyr34 and Lys39, the middle polar binding region having Arg124 and Gln125, the bottom polar binding surface with Asp129, as well as the extended polar surface consisting of Trp210 and Asp281 (Fig. 5**C**). Thus compound **14** lost all interactions with nearby residues even with a high glide docking score (−6.41). Relative to compound **14**, the docking pose of compound **15** also moved upward (Fig. 5**D**). However, replacement of the cyano group with the carboxylic acid group completely turned the ring B of compound **15** away from the polar region and shifted the aliphatic ring A inside and off the bottom hydrophobic region. The glide docking score (−5.47) of compound **15** further indicated that the addition of the carboxylic acid group was not ideal for activity against LPAR1. The active compounds, **10** and **11**, were then tested for water solubility and yielded water solubility > 100 μg/ml.

2.3. Development of QSAR model for ATX inhibitory activity prediction

Table SI-1 shows the chemical structure and QSAR parameters including the molecular weight, structural formulas, and IC_{50} values of compounds that were investigated out of 25 potential ATX inhibitor candidates. These compounds include the four newly synthesized compounds from this study and 21 compounds from our previous report [13]. The summary of the PCA of QSAR showing the *score plot* of the first principal component (*PC1*) versus the second principal component (*PC2*) for all of our compounds is presented in Fig. 6. The first *PC* accounted for 99% of the variability in the QSAR and ATX enzyme inhibition of the candidates. The second *PC* explained 1% of the variability in the candidate QSAR and ATX enzyme inhibitors. Accordingly, two *PCs* were sufficient for QSAR analysis. A detailed inspection of the *score plot* showed grouping of the ATX inhibitor candidates into four main categories. The serial number (**SL**) of the compounds from Table SI-1 has been used to represent each compound. The first grouping was

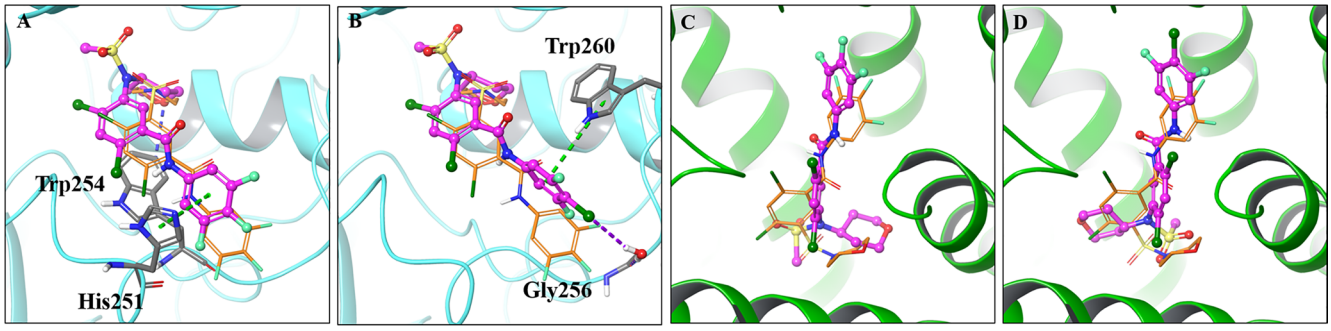

Fig. 4. Molecular modeling studies of compound **10** (A, glide docking score of −7.38) and compound **11** (B, glide docking score of −7.23) against the ATX ligand binding site (PDB ID: 3NKM), and molecular modeling studies of compound **10** (C, glide docking score of −5.98) and compound **11** (D, glide docking score of −6.23) against LPAR1 ligand binding site (PDB ID: 4Z35). Compounds **10** and **11** are shown in pink ball-and-stick model, reference compound **1** is shown in gold tube, ATX binding site is shown in cyan ribbon and LPAR1 binding site is shown in green ribbon. π-π stacking is shown in green dash line, hydrogen bond is shown in blue dash line and halogen bond is shown in purple dash line. (For interpretation of the references to color in this figure legend, the reader is referred to the web version of this article.)

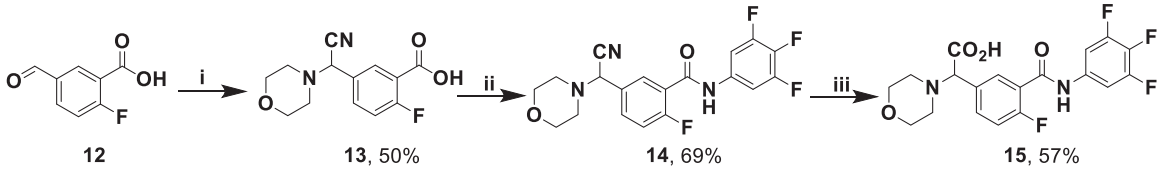

i. Morpholine, TMSCN, CH_3Cl (sol), R.T. 12 hrs; ii. a) $SOCl_2$, DMF, CH_2Cl_2, R.T. 1 hr (cat), b) 3,4,5-trifluoroaniline, R.T. 12 hrs; iii. HCl, H_2O/dioxane (1:1), 80 ^{O}C, 12 hrs

Scheme 2. Strecker method inspired design and synthesis of phenyl-glycine analogues.

observed in the left corner of the third and fourth quadrant of the *score plot*. This group (**SL5**, **SL6**, **SL7**, **SL8**, **SL9**, and **SL11**) is made up of highly potent ATX inhibitors, with an ATX enzyme inhibition IC_{50} ranging between 9 and 100 nM. The second grouping in the *score-plot* contained less potent ATX inhibitors (**SL1**, **SL2**, and **SL10**), with IC_{50} values ranging between 190 and 220 nM. Weakly potent ATX inhibitors (**SL**, ATX enzyme IC_{50} 395 nM and **SL15**, ATX enzyme IC_{50} 864 nM) are grouped diagonally on the *score plot*. Interestingly, all inactive candidates (**SL3, SL4, SL 16, SL17, SL18, SL21, SL22, SL23, SL25,** and **SL24**), with $IC_{50} \geq 1000$ nM, were grouped in the far-right hand side of the first and second quadrant.

The observed ATX enzyme inhibition is highly dependent on the candidate QSAR. In general, inhibitors containing a sulfonamide group are highly potent ($IC_{50} \leq 100$ nM). However, candidates showed reduced ATX enzyme inhibition when the sulfonamide was replaced with either CN, CO_2H, or NH, demonstrating the effect of a sulfonyl group on ATX enzyme inhibition. Remarkably, candidates with the presence of two sulfonamides or a reversed sulfonamide functional group were inactive. Moreover, compounds containing benzonazole, benzimidazole, tricholobenzamide, trimethoxy-phenyl, or hydrazine were notably inactive.

The result of the PCA of QSAR of our compounds is significant and useful for fast screening and pattern recognition of ATX inhibitors. However, the overall goal of any aided or rational drug design is to predict the potency of future drug candidates mainly from their QSAR. Accordingly, PLS regression was utilized to correlate changes in QSAR (*independent or x-variables*) with pIC_{50} (dependent or *y-variables*) of the drug molecules using a full cross-validation procedure [49–50]. The developed PLS regression was validated by independent drug candidates of known ATX enzyme inhibition pIC_{50} values. The performance and the predictive ability of the developed PLS regression of pIC_{50} were evaluated and assessed by comparing the values of experimentally obtained pIC_{50} with the predicted pIC_{50} values of the validated samples by PLS regression.

The results of the PLS regression showing the predicted ATX enzyme inhibition pIC_{50} and the experimentally obtained ATX enzyme inhibition pIC_{50} of the validation compounds are shown in Table 2. The predicted ATX enzyme inhibition pIC_{50} favorably compared with the experimental pIC_{50} values with small residuals. Other studies have demonstrated the practical applications of a combined use of QSAR analysis, regression analysis, and computational modelling in small organic drug molecule synthesis [33,34,36,37,30,31].

3. Conclusions

Using molecular modeling-guided design and synthesis, we have generated four new compounds based on our previously reported ATX inhibitors **1** and **2**. Our aim was to retain the ATX inhibitory property of the hits while improving their LPAR1 inhibitory activity. We have shown in a previous report that a moderate dual inhibitor of ATX/LPAR1, **2**, has outperformed a predominant ATX inhibitor, **1**, in a cell viability assay against a 4 T1 breast cancer cell line with high expression of both ATX and LPAR1 receptors. Our synthesis campaign was not successful at making dual inhibitors but led to two new 5-methyl-sulfonamido-5-tetrahydropyrano-aniline ATX inhibitors, **10** and **11**, with good ATX inhibition activity, 219 nM and 218 nM respectively. The combined use of QSAR and chemometric approaches in this study is highly significant for rational drug design. This set of ATX inhibitors allowed the QSAR and chemometric modeling that showed a strong correlation with the experimental findings. It will facilitate fast screening and accurate prediction of the pharmacological activity of structurally related drug candidates of substituted fragments on the scaffold prior to actual laboratory syntheses. The ability to predict the pharmacological activity and potency of structurally related drug candidates is highly desirable and attractive in rational drug design, and should significantly reduce the cost and time of synthesis of small drug molecules in drug discovery.

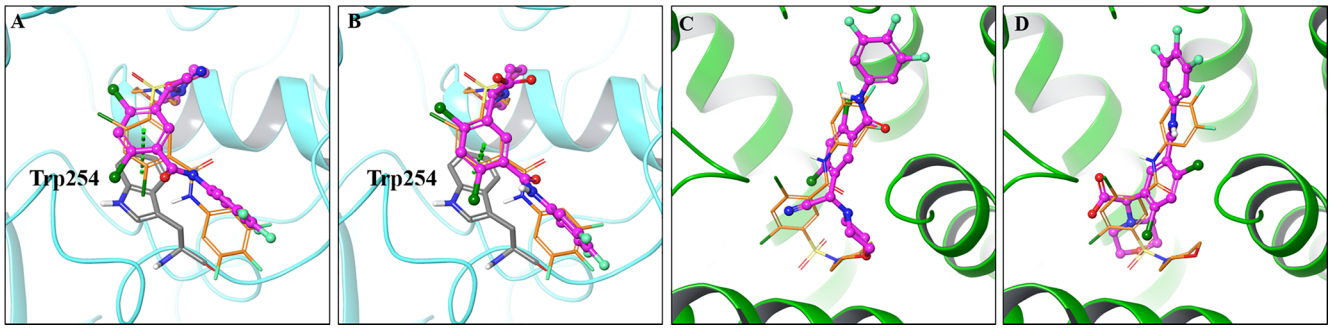

Fig. 5. Molecular modeling studies of compound **14** (A, glide docking score of −6.61) and compound **15** (B, glide docking score of −5.78) against the ATX ligand binding site (PDB ID: 3NKM), and molecular modeling studies of compound **14** (C, glide docking score of −6.41) and compound **15** (D, glide docking score of −5.47) against LPAR1 ligand binding site (**PDB ID: 4Z35**). Compounds **14** and **15** are shown in pink ball-and-stick model, reference compound **1** is shown in gold tube, ATX binding site is shown in cyan ribbon and LPAR1 binding site is shown in green ribbon. π-π stacking is shown in green dash line. (For interpretation of the references to color in this figure legend, the reader is referred to the web version of this article.)

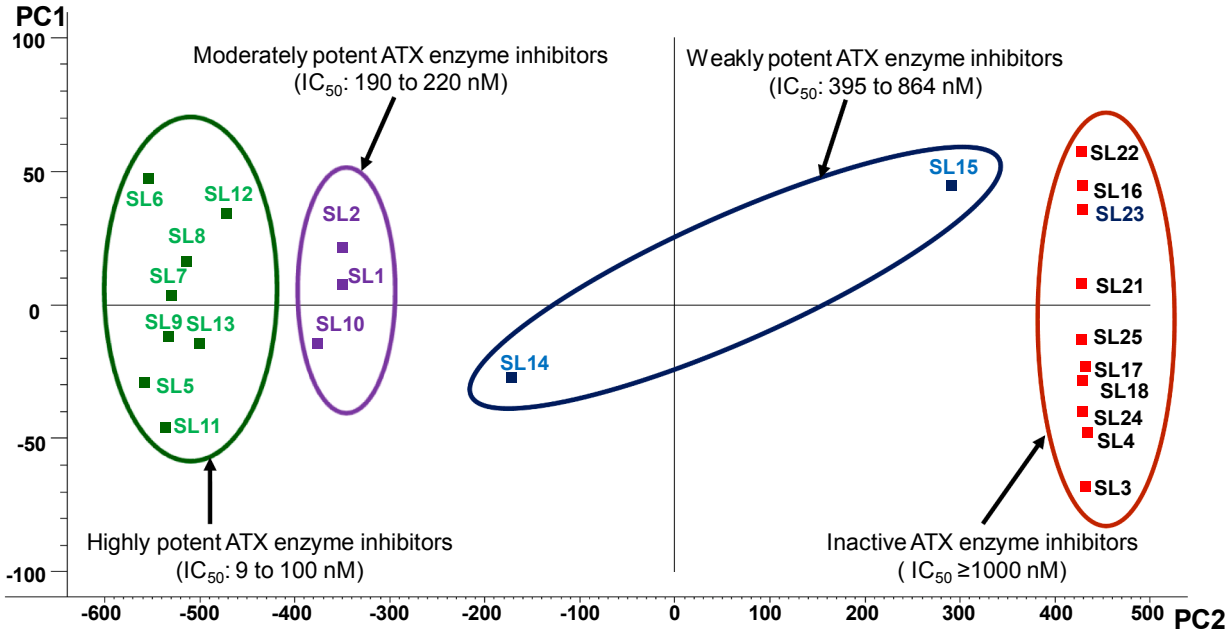

Fig. 6. Score plot of PCA of QSAR of drug candidates.

4. Experimental

4.1. Chemistry

General methods. All nonaqueous reactions were performed in oven-dried glassware under an inert atmosphere of dry nitrogen. All reagents and solvents were purchased from Aldrich (St. Louis, MO), Alfa-Aesar (Ward Hill, MA), Combi-Blocks (San Diego, CA), or Ark Pharm (Libertyville, IL) and used without further purification. Analytical thin-layer chromatography was performed on Silica Gel GHLF 10 × 20 cm Analtech TLC Uniplates (Analtech, Newark, DE) and visualized by fluorescence quenching under UV light. A Biotage SP1 flash chromatography purification system (Charlotte, NC) (Biotage SNAP cartridge, silica, 50 g and 100 g) was used to purify the compounds. 1H and 13C NMR spectra were recorded on a Varian Inova-500 spectrometer (500 MHz) (Agilent Technologies, Santa Clara, CA) or a Bruker Ascend 400 (400 MHz) (Billerica, MA) spectrometer. Chemical shifts are reported in ppm on the δ scale and referenced to the appropriate solvent peak. Mass spectra were collected on a Bruker ESQUIRE electrospray/ion trap instrument in the positive and negative modes. High-resolution mass spectrometry (HRMS) data were acquired on a Waters Xevo G2-S QTOF (Milford, MA) system equipped with an Acquity I-class UPLC system. The purity of all tested compounds was determined to be > 95% by ^{1}H NMR and HPLC. The HPLC method used to determine purity was as follows: Compound purity was analyzed using an Agilent 1100 HPLC system (Santa Clara, CA) with a Zorbax SB-C18 column, particle size 3.5 µm, 4.6 × 150 mm, from Agilent. Mobile phases consisted of water with 0.1% formic acid (A) and acetonitrile with 0.1% formic acid (B). A flow rate of 1 mL/min was used. The gradient elution started at 50% B. It reached 100% B from 0 to 9 min, was maintained at this level from 9 to 12 min, and was then decreased to 50% B from 12 to 15 min and stopped. Compound purity was monitored with a DAD detector set at 254 nm.

4.1.1. Synthesis of Methyl-5-bromo-2,4-dichloro-benzoic acid (6)

An amount of 1.7 g (6.2 mmol) of commercially available 5-bromo-2,4-dichloro-benzoic acid **(5)** was dissolved in 100 mL of Methanol. An amount of 1.2 g pTSA (6.2 mmol) was added to the solution. The reaction mixture was refluxed under argon atmosphere overnight, at which point the reaction was found to be completed as evident by TLC. The reaction mixture was diluted with 400 mL of DI waster and extracted with EtOAc (100 mL × 3). The combined EtOAc layer was dried over $MgSO_4$ and the rotary evaporated to dryness to obtain 1.6 g pure product as off white solid (5.6 mmol, 90%). ^{1}H NMR (400 MHz, $CDCl_3$). δ 8.13 (s, 1H), 7.57 (s, 1H), 3.94 (s, 3H).

4.1.2. Synthesis of methyl 2,4-dichloro-5-((tetrahydro-2H-pyran-4-yl) amino) benzoate (7)

A mixture of compound **6** (1.4 g, 4.9 mmol), 4-aminotetrahydropyran (0.74 g, 7.3 mmol), cesium carbonate (3.9 g, 12.2 mmol), Xantphos (28 mg, 0.049 mmol), and tris-(dibenzylideneacetone) dipalladium (0) (45 mg, 0.049 mmol) in 100 mL of anhydrous 1,4-dioxane was stirred at 80 °C under argon atmosphere for 18 h. Upon cooling at room temperature, the reaction mixture was filtered through a celite bed. The residue was washed with EtOAc (150 mL). The combined filtrate was extracted with water (100 mL × 10), washed with 100 mL 10% HCl, washed with brine, dried over $MgSO_4$ and evaporated to dryness. The Crude was purified in flash chromatography using 30% EtOAc/ hexanes to give 0.91 g of pure product as light yellowish solid. (3 mmol, 61%). ^{1}H NMR (400 MHz, $CDCl_3$) δ 7.36 (s, 1H), 7.09 (s, 1H), 4.26 (d, J = 8.0 Hz, 1H), 4.02 (dt, J = 11.7, 3.7 Hz, 2H), 3.93 (s, 3H), 3.64 – 3.49 (m, 3H), 2.04 (d, J = 12.3 Hz, 2H), 1.62 – 1.57 (m, 1H), 1.54 – 1.49 (m, 1H).

4.1.3. Synthesis of methyl 2,4-dichloro-5-(N-(tetrahydro-2H-pyran-4-yl)-methylsulfonamido)-benzoate (8)

An amount of 0.85 g (2.8 mmol) of compound **7** was dissolved in 50 mL of anhydrous THF under argon atmosphere. The solution was cooled down to −10 °C. A volume of 5.6 mL of 1.0 M LDA in THF (5.6 mmol) was added to the solution. The solution was stirred for 30 min at which point 310 µL of methanesulfonyl chloride (3.9 mmol) was added to the solution. The solution was stirred at −10 °C for an hour and then allowed to stir at room temperature over the night at which point it was observed to be completed as suggested by TLC. The reaction mixture was diluted with water and extracted with EtOAc (100 mL X 3). The combined EtOAc layer was washed with 10% HCl, brine and dried over $MgSO_4$ and evaporated to dryness. The Crude was purified by flash chromatography (20% EtOAc/ hexanes) to provide 0.76 g (2 mmol, 71%) of product was colorless transparent liquid. The product was mostly pure with some trace of methane sulfonyl chloride.

Table 2
Predicted pIC50 and Experimental pIC50 of drug candidates.

SL	Comp ID	Structure	IC_{50} (nM) ATX enzyme	Experimental pIC50	PredictedpIC50	Residues
2	11	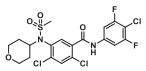	218.95	6.66	6.82	0.16
4	15	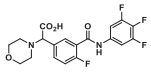	1000	6.00	5.91	−0.09
6	5	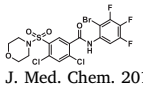 J. Med. Chem. 2017, 60, 1309–1324	17.94	7.75	8.12	0.38
8	28b	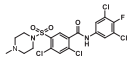 J. Med. Chem. 2017, 60, 1309–1324	55.51	7.26	7.06	−0.20
10	3 h	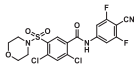 J. Med. Chem. 2017, 60, 1309–1324	190.08	6.72	7.08	0.36
12	29	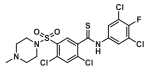 J. Med. Chem. 2017, 60, 1309–1324	100.40	7.00	7.30	0.30
14	11a	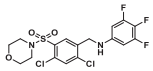 J. Med. Chem. 2017, 60, 1309–1324	395.89	6.40	6.69	0.29
16	3c	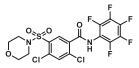 J. Med. Chem. 2017, 60, 1309–1324	1,034.16	6.00	7.92	1.92
18	7	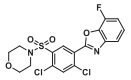 J. Med. Chem. 2017, 60, 1309–1324	1000	6.00	6.58	0.58
20	23	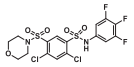 J. Med. Chem. 2017, 60, 1309–1324	1000	6.00	7.50	1.50
22	3d	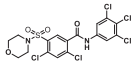 J. Med. Chem. 2017, 60, 1309–1324	1000	6.00	7.56	1.56
24	25	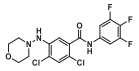 J. Med. Chem. 2017, 60, 1309–1324	1000	6.00	6.51	0.51

The product was taken for next step without further purification. ^{1}H NMR (400 MHz, $CDCl_3$) δ 7.36 (s, 1H), 7.09 (s, 1H), 4.26 (d, J = 7.8 Hz, 1H), 4.03 (t, J = 3.6 Hz, 1H), 4.00 (t, J = 3.6 Hz, 1H), 3.93 (s, 3H), 3.77 (p, J = 6.9 Hz, 1H), 3.64 – 3.48 (m, 2H), 2.05 (d, J = 11.7 Hz, 2H), 1.58 (s, 4H).

4.1.4. Synthesis of 2,4-dichloro-5-(N-(tetrahydro-2H-pyran-4-yl) methylsulfonamido) benzoic acid (9)

An amount of 0.7 g (1.8 mmol) of compound **8** was dissolved in 50 mL 1:1 THF/H2O mixture. An amount of 86 mg (3.6 mmol) of LiOH was added to the solution. The reaction was continued for 20 h at room temperature. Reaction mixture was acidified to pH 6 using 20% HCl and extracted with EtOAc (3 X 50 mL). The organic layer was washed with water, brine, dried over $MgSO_4$, and evaporated to dryness to give 0.48 g of compound **9** as colorless sticky substance. The product was taken for next step without further purification.

4.1.5. 2,4-dichloro-5-(N-(tetrahydro-2H-pyran-4-yl)-methylsulfonamido)-N-(3,4,5-trifluorophenyl)-benzamide (10)

An amount of 0.2 g (0.5 mmol) of compound **9** was dissolved in 25 mL of anhydrous methylene chloride. A volume of 158 μL of thionyl chloride (2 mmol) and catalytic amount of DMF (3–4 drops) were added to the solution. The reaction was allowed to continue under argon atmosphere for 30 min. An amount of 110 mg 3,4,-trifluro-aniline (0.75 mmol) and a volume of 274 μL of DIPEA (3 mmol) were added to the solution. The solution was allowed to react over 12 h. The reaction mixture was diluted with water, acidified to pH 6 by 10% HCl, extracted with methylene chloride (3 X 50 mL). The organic layer was washed with water, brine, dried over $MgSO_4$, and evaporated to dryness. The crude was purified by flash chromatography (1%-2% MeOH/CH_2Cl_2) to provide 180 mg of pure product as transparent sticky liquid (0.36 mmol, 72%). ^{1}H NMR (400 MHz, $CDCl_3$) δ 8.46 (s, 1H), 7.66 (d, J = 5.9 Hz, 2H), 7.40 (dd, J = 8.8, 6.1 Hz, 2H), 4.18 (td, J = 12.0, 5.9 Hz, 1H), 3.97 (td, J = 12.5, 4.9 Hz, 2H), 3.44 (td, J = 11.9, 4.8 Hz, 2H), 3.13 (s, 3H), 2.02 (dd, J = 26.5, 12.5 Hz, 2H), 1.79 (td, J = 12.0, 4.6 Hz, 1H), 1.49 (qd, J = 12.4, 4.7 Hz, 1H). HRMS [$C_{19}H_{17}Cl_2F_3N_2NaO_4S^+$]: calcd 519.0136, found 519.0142.

4.1.6. 2,4-dichloro-N-(4-chloro-3,5-difluorophenyl)-5-(N-(tetrahydro-2H-pyran-4-yl)-methylsulfonamido)-benzamide (11)

An amount of 0.2 g (0.5 mmol) of compound **9** was dissolved in 25 mL of anhydrous methylene chloride. A volume of 158 μL of thionyl chloride (2 mmol) and catalytic amount of DMF (3–4 drops) were added to the solution. The reaction was allowed to continue under argon atmosphere for 30 min. An amount of 123 mg 4-Chloro-2,5,-difluro-aniline (0.75 mmol) and a volume of 274 μL of DIPEA (3 mmol) were

added to the solution. The solution was allowed to react over 12 h. The reaction mixture was diluted with water, acidified to pH 6 by 10% HCl, extracted with methylene chloride (3 × 50 mL). The organic layer was washed with water, brine, dried over $MgSO_4$, and evaporated to dryness. The Crude was purified by flash chromatography (1%-2% MeOH/CH_2Cl_2) to provide 195 mg of pure product as transparent sticky liquid (0.38 mmol, 76%). ^{1}H NMR (400 MHz, $CDCl_3$) δ 8.34 (s, 1H), 7.61 (d, J = 14.9 Hz, 2H), 7.34 (d, J = 8.4 Hz, 2H), 4.13 (tt, J = 12.0, 4.1 Hz, 1H), 3.91 (ddd, J = 16.1, 11.9, 4.5 Hz, 2H), 3.38 (tdd, J = 11.9, 4.9, 2.1 Hz, 2H), 3.06 (s, 3H), 2.02 – 1.89 (m, 2H), 1.70 (qd, J = 12.0, 4.6 Hz, 1H), 1.42 (qd, J = 12.4, 4.7 Hz, 1H). HRMS [$C_{19}H_{17}Cl_3F_2N_2NaO_4S^+$]: calcd 534.9840, found 534.9851.

4.1.7. Synthesis of 5-(cyano(morpholino)methyl)-2-fluorobenzoic acid (13)

A mixture of compound **12**, 2-fluoro-5-formyl-benzoic acid, (0.2 g 1.2 mmol), morpholine (100 μL, 1.2 mmol), $Zn(OAc)_2$. $2H_20$ (Catalytic amount), and TMS-CN (0.131 g, 1.3 mmol) in chloroform (50 mL) was stirred in room temperature over 12 h. The reaction mixture was diluted with water and extracted with methylene chloride (3 X 50 mL). The organic layer was washed with water, brine, dried over MgSO4, and evaporated to dryness to yield 158 mg (0.6 mmol, 50%) crude. The Crude was taken for the next step without further purification.

4.1.8. 5-(cyano(morpholino)methyl)-2-fluoro-N-(3,4,5-trifluorophenyl)-benzamide (14)

An amount of 0.120 g (0.45 mmol) of compound **13** was dissolved in 25 mL of anhydrous methylene chloride. A volume of 158 μL of thionyl chloride (2 mmol) and catalytic amount of DMF (3–4 drops) were added to the solution. The reaction was allowed to continue under argon atmosphere for 30 min. An amount of 123 mg 4-Chloro-2,5, -difluro-aniline (0.75 mmol) and a volume of 274 μL of DIPEA (3 mmol) were added to the solution. The solution was allowed to react over 12 h. The reaction mixture was diluted with water, acidified to pH 6 by 10% HCl, extracted with methylene chloride (3 × 50 mL). The organic layer was washed with water, brine, dried over $MgSO_4$, and evaporated to dryness. The crude was purified by flash chromatography (40%-60% EtOAc/hexanes) to provide 122 mg of pure product as white solid (0.31 mmol, 69%). ^{1}H NMR (400 MHz, DMSO-d_6) δ 10.86 (s, 1H), 7.77 – 7.59 (m, 4H), 7.51 (dd, J = 9.8, 8.6 Hz, 1H), 3.64 (m, 4H), 2.57 (m, 2H), 2.47 – 2.37 (m, 2H). HRMS [$C_{19}H_{15}F_4N_3NaO_2^+$]: calcd 416.0998, found 416.0999

4.1.9. Synthesis of 2-(4-fluoro-3-((3,4,5-trifluorophenyl)-carbamoyl)-phenyl)-2-morpholinoacetic acid (15)

An amount of 75 mg of compound **14** (0.19 mmol) was dissolved in 10 mL of 1:1 dioxane/H_2O mixture. A volume of 3 mL of conc. HCl was added in a dropwise manner. The mixture was heated at 80 °C for 12 h. The reaction was neutralized to pH 6.8. The reaction mixture was extracted with methylene chloride (3 X 50 mL), washed with water, brine, dried over $MgSO_4$, and evaporated to dryness. The crude was purified by flash chromatography (2% MeOH in CH_2Cl_2) to yield 45 mg pure product (0.11 mmol, 57%) as colorless sticky liquid. ^{1}H NMR (400 MHz, DMSO-d_6) δ 9.53 (bs, 2H), 7.94–6.86 (m, 5H), 5.77 (s, 1H), 3.84–3.77 (m, 4H), 3.10–3.03 (m, 4H). HRMS [$C_{19}H_{15}F_4N_2O_4^-$]: calcd 411.0968, found 411.0973.

4.2. Molecular modelling

The crystal structures of ATX (PDB ID: 3NKM) and LPAR1 (PDB ID: 4Z35) were obtained from Protein Data Bank. The ligand structures were built and prepared by using the LigPrep tool of modeling software Schrödinger Molecular Modeling Suite 2019 (Schrödinger LLC, New York, NY). The proteins were preprocessed by adding hydrogens, filling the missing chains, optimizing hydrogen bonds, and minimizing energy using Protein Preparation Wizard workflow with procedures similar to those described before [51]. The receptor grid of 3NKM was generated by centering the binding site enclosing box on the major residues at the active binding site, including Lys39, Arg124, and Glu293, using the Receptor Grid Generation. The receptor grid of LPAR1 was generated with a grid box centered on the active ligand-binding site. Then the standard precision of flexible molecular docking was performed by using the Glide Docking module. The binding modes of the ligands and data analysis were carried out using Maestro. The glide docking score generated in the docking represents an estimated binding energy when a ligand binds to the receptor. A lower ligand glide docking score normally demonstrates a more favorable binding interaction with the receptor.

4.3. Testing of ATX inhibitors on ATX and LPAR

4.3.1. Generation of recombinant ATX

Human recombinant ATX was expressed as published previously, using Sf9 *Spodoptera frugiperda* ovary cells (Invitrogen, Carlsbad, CA). [8] Suspension cells were grown to a 1 L quantity at a concentration of 1 × 10^6 cells/mL in Sf-900 III serum-free medium (Invitrogen) supplemented with 50 U/mL penicillin and 50 μg/mL streptomycin at 27 °C with agitation. Cells were then infected with high-titer baculovirus generated via the Bac-to-Bac baculovirus expression system (Invitrogen) using the pCMV5 mammalian expression vector containing a C-terminal FLAG-tagged human ATX sequence (a generous gift from Dr. Junken Aoki, Tohoku University, Sendai, Japan) subcloned into the pFastBac1 transfer vector. Expression was allowed to proceed for 72 h, and secreted protein was harvested by centrifugation and filtration of the culture medium followed by affinity chromatography using anti-FLAG M2 agarose beads (Sigma-Aldrich, St. Louis, MO) and competitive elution with 50 μg/mL FLAG peptide (Sigma-Aldrich). Resultant ATX was then concentrated via centrifugation in Amicon Ultra 30 000 molecular weight cut off filter units (Millipore, Billerica, MA) and subsequent buffer exchange into storage buffer composed of 50 mM Tris, pH 7.4, with 20% (v/v) ethylene glycol. Protein was held at −80 °C for long-term storage.

4.3.2. ATX inhibition

ATX activity was assessed via hydrolysis of the synthetic lipid-like FRET-based substrate FS-3 (Echelon Biosciences, Salt Lake City, UT) or via hydrolysis of the nucleotide substrate p-nitrophenyl thymidine 5′-monophosphate (pNPTMP) as described previously [9]. Reaction wells were loaded in 60 μL volumes in triplicate wells of black-wall 96-well plates in assay buffer consisting of 50 mM Tris, 140 mM NaCl, 5 mM KCl, 1 mM $CaCl_2$, 1 mM $MgCl_2$, 10 μM BSA, pH 8.0 for ATX. For dose − response and IC_{50} generation, final concentrations per reaction well were composed of 1 μM FS-3 (or 1 mMpNP-TMP), 0 or 4 nM human rATX, and test compound concentrations ranging from 0 to 1 μM. To determine the mechanism of action, triplicate wells were loaded with assay buffer with FS-3 concentrations ranging from 0 to 10 μM, 0 or 4 nM ATX, and inhibitor concentrations of 0, 0.5 × IC_{50}, or 2 × IC_{50}. Fluorescence was read every 2 min for 1 h at excitation/emission wavelengths of 485/528 nm for FS-3 hydrolysis or 405 nm absorbance for pNP-TMP or pNPPC hydrolysis using a FlexStation 3 microplate reader (Molecular Devices, Sunnyvale, CA). Data (relative fluorescence or absorbance) were then recorded as a mean value of the triplicates for each sample versus time. Percent ATX activity (± SD) were calculated from the 1 h time point data for each inhibitor concentration, and GraphPad Prism version 5.0a (GraphPad Software, San Diego, CA) was then used to fit nonlinear regression curves, fitting the Hill slope from the data in a variable slope model and interpolating from the curve to determine the IC_{50} (± SD) for each compound. In the case of mechanism determination, the linear fluorescence data from 10 to 30 min were then transformed using a carboxyfluorescein standard curve to determine product concentration and plotted separately. Linear trend lines were inserted using Microsoft Excel, the slope of

which represents the rates of reaction for each substrate concentration. This reaction rate data for each inhibitor concentration was then plotted against substrate (FS-3) concentration and simultaneously fitted via nonlinear regression in the Michaelis − Menten equations for competitive, noncompetitive, uncompetitive, and mixed-mode inhibition using GraphPad Prism, version 5.0a. The mechanism of inhibition was identified by determining which curve had the best global fit (R^2 value).

4.3.3. Dose response relationship of LPA1 receptor inhibition by 11 and 12

As published previously, LPAR activation leads to transient calcium mobilization. In order to assess receptor activation or antagonism, compounds were tested in stable transfectant cell lines engineered to overexpress LPA1 [19] LPA1 RH7777 rat hepatoma cells were generated in-house as described previously [52] and maintained in DMEM supplemented with 10% FBS and 2 mM L-glutamine with 250 μg/mL G418. Cells were maintained at 37 °C with 5% CO_2 in a humidified atmosphere. Calcium mobilization was assessed via fluorescence in Fura-2AM-loaded cells treated with a dose range of test compound both in the absence and presence of the EC_{50} concentration of LPA 18:1. Cells were plated in triplicate in poly-L-lysine coated 96-well, black-wall plates at a density of 5×10^4 cells per well and allowed to adhere overnight. After adherence, cells were serum-deprived for 4 h in Krebs buffer consisting of 10 mM HEPES, pH 7.4, with 120 mM NaCl, 5 mM KCl, 1.8 mM $CaCl_2$, 0.62 mM $MgSO_4$, and 6 mM D-glucose. Fura-2AM was then loaded for 30 min at a concentration of 4.5 μg/mL in Krebs buffer with 0.45% (v/v) Pluronic F-127, after which cells were switched to fresh Krebs buffer. Finally, a FlexStation 3 microplate reader was used to apply a dose range of LPA 18:1 (in a 1:1 molecular complex with lipid-depleted BSA) or test compounds ranging from 0 to 100 μM in the presence and absence of the EC_{50} concentration of LPA 18:1. Fluorescence corresponding to calcium mobilization was immediately monitored upon addition every 3.42 s over a span of 70 s at excitation/emission wavelengths of 340/510 and 380/510 nm. Data (relative fluorescence) were then recorded as a mean fluorescence ratio value of the triplicates for each concentration and normalized to percentage of LPA 18:1 Emax. GraphPad Prism, version 5.0a, was then used to plot the data and fit nonlinear regression curves in a variable slope model in order to determine the pharmacodynamics (EC_{50} or IC_{50}) of the compounds in Ca^{2+} mobilization.

4.4. QSAR analysis, principal component analysis (PCA), and partial-least-square (PLS) regression analysis

Table SI-1 shows the chemical structure and QSAR including the molecular weight (MW); number of C, H, Cl, O, S, N, F, and Br atoms; number of double bonds (DB); and experimentally obtained IC_{50} of the investigated of potential 25 drug candidates. The IC_{50} of each drug candidate was first converted to pIC_{50} (-log IC_{50}) and subsequently utilized as dependent (*y*-variables) for partial-least-square (PLS) regression analysis. In the initial stage of the study, QSAR of drug candidates was subjected to PCA for pattern recognition. In the second stage of the study, the data set in Table SI-1 was randomly divided into two data set. One data set was utilized as the "*training set*" for PLS regression model development. PLS regression was utilized to correlate changes in QSAR (*independent or x-variables*) with pIC_{50} (dependent or *y-variables*) of the drug candidates using a full cross validation approach [53–56]. The developed PLS regression was validated by independent drug candidates. The performance and the predictive ability of the developed PLS regression was evaluated and assessed by comparing the experimentally obtained pIC_{50} with the predicted pIC_{50} values of the validated samples. QSAR, PCA and PLS regression analysis were performed using commercially available chemometric software, The Unscrambler Chemometrics software (CAMO Software, 9.8, Oslo, Norway).

Declaration of Competing Interest

The authors declare that they have no known competing financial interests or personal relationships that could have appeared to influence the work reported in this paper.

Acknowledgements

This research was supported by the NIH/NCI Grants (CA-092160) to Drs. Gabor G. Tigyi and Duane D. Miller as well as the Arkansas INBRE Voucher award to Dr. Souvik Banerjee. We thank the Department of Physical Sciences at the UAFS for instrument grants used to obtain the mass spectrometry and NMR facilities used in conducting this research. We thank the Dean's office at the UAFS for providing us with some necessary chemicals to carry out the synthesis. We also thank the Department of Physical Sciences at the UAFS for continued support of our research programs. Finally, we would like to thank Ms. Amada S. Clarke for editing this manuscript.

Appendix A. Supplementary material

^{1}H NMR of the intermediate and target compounds. Supplementary data to this article can be found online at https://doi.org/10.1016/j.bioorg.2020.104188.

References

[1] H.M.H.G. Albers, L.J.D. Hendrickx, R.J.P. van Tol, J. Hausmann, A. Perrakis, H. Ovaa, Structure-based design of novel boronic acid-based inhibitors of autotaxin, J. Med. Chem. 54 (2011) 4619–4626.
[2] H.M.H.G. Albers, H. Ovaa, Chemical evolution of autotaxin inhibitors, Chem. Rev. 112 (2012) 2593–2603.
[3] H.M.H.G. Albers, L.A. van Meeteren, D.A. Egan, E.W. van Tilburg, W.H. Moolenaar, H. Ovaa, Discovery and optimization of boronic acid based inhibitors of autotaxin, J. Med. Chem. 53 (2010) 4958–4967.
[4] E. Barbayianni, E. Kaffe, V. Aidinis, G. Kokotos, Autotaxin, a secreted lysophospholipase D, as a promising therapeutic target in chronic inflammation and cancer, Prog. Lipid Res. 58 (2015) 76–96.
[5] E. Barbayianni, V. Magrioti, P. Moutevelis-Minakakis, G. Kokotos, Autotaxin inhibitors: a patent review, Expert Opin. Ther. Pat. 23 (2013) 1123–1132.
[6] D. Castagna, D.C. Budd, S.J.F. Macdonald, C. Jamieson, A.J.B. Watson, The development of autotaxin inhibitors: an overview of the patent and primary literature, J. Med. Chem. 59 (2016) 5604–5621.
[7] D. Castagna, E.L. Duffy, D. Semaan, L.C. Young, J.M. Pritchard, S.J.F. Macdonald, D.C. Budd, C. Jamieson, A.J.B. Watson, Identification of a novel class of autotaxin inhibitors through cross-screening, Med. Chem. Commun. 6 (2015) 1149–1155.
[8] J.I. Fells, S.C. Lee, Y. Fujiwara, D.D. Norman, K.G. Lim, R. Tsukahara, J. Liu, R. Patil, D.D. Miller, R.J. Kirby, S. Nelson, W. Seibel, R. Papoian, A.L. Parrill, D.L. Baker, R. Bittman, G. Tigyi, Hits of a high-throughput screen identify the hydrophobic pocket of autotaxin/lysophospholipase D as an inhibitory surface, Mol. Pharmacol. 84 (2013) 415–424.
[9] J.I. Fells, S.C. Lee, D.D. Norman, R. Tsukahara, J.R. Kirby, S. Nelson, W. Seibel, R. Papoian, R. Patil, D.D. Miller, A.L. Parrill, T.-C. Pham, D.L. Baker, R. Bittman, G. Tigyi, Targeting the hydrophobic pocket of autotaxin with virtual screening of inhibitors identifies a common aromatic sulfonamide structural motif, FEBS J. 281 (2014) 1017–1028.
[10] M. Gotoh, Y. Fujiwara, J. Yue, J. Liu, S. Lee, J. Fells, A. Uchiyama, K. Murakami-Murofushi, S. Kennel, J. Wall, R. Patil, R. Gupte, L. Balazs, D.D. Miller, G.J. Tigyi, Controlling cancer through the autotaxin–lysophosphatidic acid receptor axis, Biochem. Soc. Trans. 40 (2012) 31–36.
[11] R. Gupte, R. Patil, J. Liu, Y. Wang, S.C. Lee, Y. Fujiwara, J. Fells, A.L. Bolen, K. Emmons-Thompson, C.R. Yates, A. Siddam, N. Panupinthu, T.-C.-T. Pham, D.L. Baker, A.L. Parrill, G.B. Mills, G. Tigyi, D.D. Miller, Benzyl and naphthalene methylphosphonic acid inhibitors of autotaxin with anti-invasive and anti-metastatic activity, ChemMedChem 6 (2011) 922–935.
[12] A.B. Hoeglund, H.E. Bostic, A.L. Howard, I.W. Wanjala, M.D. Best, D.L. Baker, A.L. Parrill, Optimization of a pipemidic acid autotaxin inhibitor, J. Med. Chem. 53 (2010) 1056–1066.
[13] S. Banerjee, D.D. Norman, S.C. Lee, A.L. Parrill, T.C.T. Pham, D.L. Baker, G.J. Tigyi, D.D. Miller, Highly potent non-carboxylic acid autotaxin inhibitors reduce melanoma metastasis and chemotherapeutic resistance of breast cancer stem cells, J. Med. Chem. 60 (2017) 1309–1324.
[14] D.N. Brindley, F.-T. Lin, G.J. Tigyi, Role of the autotaxin-lysophosphatidate axis in cancer resistance to chemotherapy and radiotherapy, Biochim. Biophys. Acta. 1831 (2013) 74–85.
[15] J.W. Choi, D.R. Herr, K. Noguchi, Y.C. Yung, C.-W. Lee, T. Mutoh, M.-E. Lin, S.T. Teo, K.E. Park, A.N. Mosley, J. Chun, LPA receptors: subtypes and biological

actions, Annu. Rev. Pharmacol. Toxicol. 50 (2010) 157–186.
[16] K. Kraljić, D. Jelić, D. Žiher, A. Cvrtila, S. Dragojević, V. Sinković, M. Mesić, Benzoxaboroles—novel autotaxin inhibitors, Molecules 24 (2019) 3419.
[17] S.B. Jones, L.A. Pfeifer, T.J. Bleisch, T.J. Beauchamp, J.D. Durbin, V.J. Klimkowski, N.E. Hughes, C.J. Rito, Y. Dao, J.M. Gruber, H. Bui, M.G. Chambers, S. Chandrasekhar, C. Lin, D.J. McCann, D.R. Mudra, J.L. Oskins, C.A. Swearingen, K. Thirunavukkarasu, B.H. Norman, Novel autotaxin inhibitors for the treatment of osteoarthritis pain: lead optimization via structure-based drug design, ACS Med. Chem. Lett. 7 (2016) 857–861.
[18] S.-C. Lee, Y. Fujiwara, J. Liu, J. Yue, Y. Shimizu, D.D. Norman, Y. Wang, R. Tsukahara, E. Szabo, R. Patil, S. Banerjee, D.D. Miller, L. Balazs, M.C. Ghosh, C.M. Waters, T. Oravecz, T.G.J. Autotaxin, LPA receptors (1 and 5) exert disparate functions in tumor cells versus the host tissue microenvironment in melanoma invasion and metastasis, Mol. Cancer Res. (2014).
[19] H. Zhang, X. Xu, J. Gajewiak, R. Tsukahara, Y. Fujiwara, J. Liu, J.I. Fells, D. Perygin, A.L. Parrill, G. Tigyi, G.D. Prestwich, Dual activity lysophosphatidic acid receptor pan-antagonist/autotaxin inhibitor reduces breast cancer cell migration in vitro and causes tumor regression in vivo, Cancer Res. 69 (2009) 5441–5449.
[20] M.G.K. Benesch, I.T.K. MacIntyre, T.P.W. McMullen, D.N. Brindley, Coming of age for autotaxin and lysophosphatidate signaling: clinical applications for preventing, detecting and targeting tumor-promoting inflammation, Cancers 10 (2018) 73.
[21] O. Peyruchaud, L. Saier, R. Leblanc, Autotaxin implication in cancer metastasis and autoimmune disorders: functional implication of binding autotaxin to the cell surface, Cancers 12 (2020) 105.
[22] E.J. Seo, Y.W. Kwon, I.H. Jang, D.K. Kim, S.I. Lee, E.J. Choi, K.-H. Kim, D.-S. Suh, J.H. Lee, K.U. Choi, J.W. Lee, H.J. Mok, K.P. Kim, H. Matsumoto, J. Aoki, J.H. Kim, Autotaxin regulates maintenance of ovarian cancer stem cells through lysophosphatidic acid-mediated autocrine mechanism, Stem Cells 34 (2016) 551–564.
[23] Y. Xu, Targeting lysophosphatidic acid in cancer: the issues in moving from bench to bedside, Cancers 11 (2019) 1523.
[24] D. Lee, D.-S. Suh, S.C. Lee, G.J. Tigyi, J.H. Kim, Role of autotaxin in cancer stem cells, Cancer Metastasis Rev. 37 (2018) 509–518.
[25] F. Salgado-Polo, A. Perrakis, The structural binding mode of the four autotaxin inhibitor types that differentially affect catalytic and non-catalytic functions, Cancers 11 (2019) 1577.
[26] E. van der Aar, J. Desrivot, S. Dupont, B. Heckmann, A. Fieuw, S. Stutvoet, L. Fagard, K. Van de Wal, E. Helmer, Safety, pharmacokinetics, and pharmacodynamics of the autotaxin inhibitor GLPG1690 in healthy subjects: phase 1 randomized trials, J. Clin. Pharmacol. 59 (2019) 1366–1378.
[27] T.M. Maher, M. Kreuter, D.J. Lederer, K.K. Brown, W. Wuyts, N. Verbruggen, S. Stutvoet, A. Fieuw, P. Ford, W. Abi-Saab, M. Wijsenbeek, Rationale, design and objectives of two phase III, randomised, placebo-controlled studies of GLPG1690, a novel autotaxin inhibitor, in idiopathic pulmonary fibrosis (ISABELA 1 and 2), BMJ Open Respir. Res. 6 (2019) e000422.
[28] J.E. Chrencik, C.B. Roth, M. Terakado, H. Kurata, R. Omi, Y. Kihara, D. Warshaviak, S. Nakade, G. Asmar-Rovira, M. Mileni, H. Mizuno, M.T. Griffith, C. Rodgers, G.W. Han, J. Velasquez, J. Chun, R.C. Stevens, M.A. Hanson, Crystal structure of antagonist bound human lysophosphatidic acid receptor 1, Cell 161 (2015) 1633–1643.
[29] V. Srivastava, D. Sinha, K.A. Tiwari, H. Sharma, B.R. Sharma, K.V. Singh, K.A. Mishra, Quantitative structure-activity relationship analysis of 4(3H)-quinazolone derivatives as tyrosine kinase inhibitors by multiple linear regression, Cancer Biother. Radiopharm. 25 (2010) 559–562.
[30] S. Alam, F. Khan, 3D-QSAR studies on maslinic acid analogs for anticancer activity against breast cancer cell line MCF-7, Sci. Rep. 7 (2017) 6019.
[31] V. Jitender, M.K. Vijay, C.C. Evans, 3D-QSAR in drug design - a review, Curr. Top. Med. Chem. 10 (2010) 95–115.
[32] A.R. Katritzky, V.S. Lobanov, M. Karelson, QSPR: the correlation and quantitative prediction of chemical and physical properties from structure, Chem. Soc. Rev. 24 (1995) 279–287.
[33] A.K. Tiwari, H. Ojha, A. Kaul, A. Dutta, P. Srivastava, G. Shukla, R. Srivastava, A.K. Mishra, Quantitative structure-property relationship (correlation analysis) of phosphonic acid-based chelates in design of MRI contrast agent, Chem. Biol. Drug. Des. 74 (2009) 87–91.
[34] A. Cherkasov, E.N. Muratov, D. Fourches, A. Varnek, I.I. Baskin, M. Cronin, J. Dearden, P. Gramatica, Y.C. Martin, R. Todeschini, V. Consonni, V.E. Kuz'min, R. Cramer, R. Benigni, C. Yang, J. Rathman, L. Terfloth, J. Gasteiger, A. Richard, A. Tropsha, QSAR modeling: where have you been? where are you going to? J. Med. Chem. 57 (2014) 4977–5010.
[35] A.S. Edwards, D.J. Bennett, E.L. Carswell, A.J. Cooke, O. Nimz, Design, structure activity relationships and X-ray co-crystallography of non-steroidal LXR agonists, Curr. Med. Chem. 15 (2008) 195–209.
[36] J. Ling, R. Kumar, Crosstalk between NFkB and glucocorticoid signaling: A potential target of breast cancer therapy, Cancer Lett. 322 (2012) 119–126.
[37] S. Kapoor, Maslinic acid and its in vitro anti-neoplastic effects, Nat. Prod. Res. 27 (2013) 2210–2211.
[38] G. Klebe, U. Abraham, T. Mietzner, Molecular similarity indices in a comparative analysis (CoMSIA) of drug molecules to correlate and predict their biological activity, J. Med. Chem. 37 (1994) 4130–4146.
[39] H. Yuan, W. Tai, S. Hu, H. Liu, Y. Zhang, S. Yao, T. Ran, S. Lu, Z. Ke, X. Xiong, J. Xu, Y. Chen, T. Lu, Fragment-based strategy for structural optimization in combination with 3D-QSAR, J. Comput. Aided Mol. Des. 27 (2013) 897–915.
[40] A.Y. Jin, H. Kohn, C. Béguin, S.V. Andurkar, J.P. Stables, D.F. Weaver, A quantitative structure-activity relationship study for α-substituted acetamido-N-benzylacetamide derivatives A novel anticonvulsant drug class, Can. J. Chem. 83 (2005) 37–45.
[41] S. Hannongbua, P. Pungpo, J. Limtrakul, P. Wolschann, Quantitative structure-activity relationships and comparative molecular field analysis of TIBO derivatised HIV-1 reverse transcriptase inhibitors, J. Comput. Aided Mol. Des. 13 (1999) 563–577.
[42] K. Venko, Š. Župerl, M. Novič, Prediction of antiprion activity of therapeutic agents with structure–activity models, Mol. Divers. 18 (2014) 133–148.
[43] S. Funar-Timofei, A. Borota, L. Crisan, Combined molecular docking and QSAR study of fused heterocyclic herbicide inhibitors of D1 protein in photosystem II of plants, Mol. Divers. 21 (2017) 437–454.
[44] A. Speck-Planche, V.V. Kleandrova, J.A. Rojas-Vargas, QSAR model toward the rational design of new agrochemical fungicides with a defined resistance risk using substructural descriptors, Mol. Divers. 15 (2011) 901–909.
[45] M.N. Gandy, M.G. Corral, J.S. Mylne, K.A. Stubbs, An interactive database to explore herbicide physicochemical properties, Org. Biomol. Chem. 13 (2015) 5586–5590.
[46] S. Avram, S. Funar-Timofei, A. Borota, S.R. Chennamaneni, A.K. Manchala, S. Muresan, Quantitative estimation of pesticide-likeness for agrochemical discovery, J. Cheminformatics 6 (2014) 42.
[47] M.S. Karacan, Ç. Yakan, M. Yakan, N. Karacan, S.K. Zharmukhamedov, A. Shitov, D.A. Los, V.V. Klimov, S.I. Allakhverdiev, Quantitative structure–activity relationship analysis of perfluoroiso-propyldinitrobenzene derivatives known as photosystem II electron transfer inhibitors, 1817, Biochim. Biophys. Acta (BBA) - Bioenergetics (2012) 1229–1236.
[48] M. Hamadache, O. Benkortbi, S. Hanini, A. Amrane, QSAR modeling in ecotoxicological risk assessment: application to the prediction of acute contact toxicity of pesticides on bees (Apis mellifera L.), Environ. Sci. Pollut. Res. 25 (2018) 896–907.
[49] M. Otto, Pattern recognition and classification, Chemometrics (2016) 135–211.
[50] K.R. Beebe, R.J. Pell, M.B. Seasholtz, Chemometrics: A Practical Guide, John Wiley & Sons New York, NY, 1998, p. 360.
[51] Y. Lu, J. Chen, J. Wang, C.-M. Li, S. Ahn, C.M. Barrett, J.T. Dalton, W. Li, D.D. Miller, Design, synthesis, and biological evaluation of stable colchicine binding site tubulin inhibitors as potential anticancer agents, J. Med. Chem. 57 (2014) 7355–7366.
[52] T.A. Halgren, MMFF VI. MMFF94s option for energy minimization studies 20 (1999) 720–729.
[53] S. Pack, Factor analysis in chemistry, (2nd edition), E.R. Malinowski, Wiley-Interscience, 1991. ISBN 0-471-53009-3. 1991, 5, 545–545.
[54] S. De Jong, Multivariate calibration, H. Martens and T. Naes, Wiley, New York, 1989. ISBN 0 471 90979 3. No. of pages: 504. 1990, 4, 441-441.
[55] B. Slutsky, Chemometrics: A practical guide by Kenneth R. Beebe, Randy J. Pell, and Mary Beth Seasholtz. Wiley-Interscience Series on Laboratory Automation. John Wiley & Sons: New York, 1998. xi + 348 pp. ISBN 0-471-12451-6. J. Chem. Inf. Comput. Sci. 1998, 38, 1254-1254.
[56] Pattern recognition and classification. In Chemometrics, pp. 135–211.